Tunable Thermally Bistable Multi-material Structure

Hamed Niknam, Abdolhamid Akbarzadeh, Daniel Therriault and Sampada Bodkhe**

Dr. H. Niknam, Prof. D. Therriault, Prof. S. Bodkhe
Department of Mechanical Engineering, Polytechnique Montréal, Montréal, QC H3T 1J4, Canada
Research Center for High-Performance Polymer and Composite Systems (CREPEC)
E-mail: sampada.bodkhe@polymtl.ca

Prof. A.H. Akbarzadeh
Department of Bioresource Engineering, McGill University, Montreal, QC H9X 3V9, Canada
Research Center for High-Performance Polymer and Composite Systems (CREPEC)
Email: hamid.akbarzadeh@mcgill.ca

Prof. A.H. Akbarzadeh
Department of Mechanical Engineering, McGill University, Montreal, QC H3A 0C3, Canada

Keywords: Mechanical metamaterials, Bistable structures, Architected thermal actuators, Shape memory behavior

Abstract

The shape memory effect in polymers and alloys enables programming the response of structures via temperature changes; however, the number of materials exhibiting such memory behavior is limited, their response to thermal load is considerably slow, and programming is required to guide the deformation of shape memory materials. The recently revived structural bistability concept offers a potential to design and program reconfigurable structures. In this study, we introduce a thermally bistable structure that displays an abrupt shape memory effect along with snap-through instability behavior. We demonstrate the effect of the wall stiffness of the structure on the bistability of a mechanically bistable element and its nonlinear response. We utilize the thermal softening behavior of two distinct polymers to design a bistable bimaterial structure that restores its original shape when the environment reaches a specific temperature, referred to as *triggering temperature*. The results reveal that the triggering temperature can change within a range of 30℃ by changing the width ratio of the stiff material at the wall from 0 to 0.5 for specific material composition. The proposed concept offers new

opportunities to utilize tessellated bistable structures as self-sensing actuators and intelligent deployable structures since they can be designed to reconfigure in response to certain changes in temperature.

1. Introduction

As the name suggests, bistable materials and structures have two stable configurations; meaning that they can remain in a non-initial stable equilibrium after deformation. When we apply force to a deformable body and then remove it, the body either deforms permanently or restores its initial shape elastically. The permanent deformation is often irreversible since it is associated with material failure or plasticity; however, bistable structures can demonstrate reversible permanent deformation. The long-known bistability concept has been recently revived due to its potential applications in soft robots [1], deployable structures [2, 3], actuators [4, 5], and reusable energy absorbers [6]. In addition, advances in additive manufacturing (AM), e.g., fused filament fabrication (FFF) and direct writing (DW), provide the means to fabricate multistable one-dimensional and two-dimensional structures with tailored buckling for restorable shock absorbers [7, 8]. Tripple jetting technology also facilitates the fabrication of more complex torsional [9, 10] or hierarchical bistable [11] structures, which can achieve multiple activated states depending on the magnitude and direction of loading value. The variety of topologies proposed for bistable architectures paves the path for designing structures with targeted stable configurations.

Bistable structures have a binary response to loading conditions, i.e., they can have two stable configurations; initial and deformed. This binary response enables the utilization of bistable structures in the design of smart adaptive biomedical devices [12, 13]. For instance, logic gates were designed by using bistable structures made of soft elastomeric materials and embedded into robots to reduce the complexities of robots‘ design and increase their mobility [14-19]. In another work, an array of fluid-driven bistable elastic chambers connected by thin tubes were

used to reproduce logic gates controllable by the flow rate [20]. A bistable transistor-like device was designed based on geometric nonlinearities to switch between two different configurations and consequently tune the elastic vibration [21]. Creating an array of this device in a tunable mechanical circuit created a complete set of mechanical logic elements that could execute simple calculations [21]. The concept of multistability enabled the fabrication of morphing three-dimensional (3D) mesostructures, which could function in an adaptive radiofrequency circuit or concealable electromagnetic devices [22].

In the abovementioned smart structures, mechanical loading was required to trigger the transition between stable states. However, specific applications require a robot or an actuator that reacts to a non-mechanical environmental stimulus. As a result, a few investigations tried to design and fabricate bistable structures whose deformation can be controlled and programmed by magnetic [23-25], electric [4], thermal conditions [26, 27], and liquid diffusion [28]. Magnetic actuation of bistable structures allows fast transformations between complex 3D printed ferromagnetic materials [23]. The possibility of reprogramming bistable actuators through applying a magnetic field was also demonstrated through tessellated mechanical metamaterials with stable memories [24]. Reconfiguring a structure to its second stable configuration by applying an electrical field was enabled by a trilayered polymeric material containing dielectric elastomers [4]. A few studies proposed the possibility of thermal actuation of a bistable structure and demonstrated the configurational changes by altering temperature [26, 27, 29]. Origami designs were employed to facilitate active reconfiguration, triggered by temperature modulation, in architected structures with multiple stable configurations [30, 31]. Logic was also embodied in an autonomous system by the transition between bistability and monostability, and the liquid diffusion was exploited as a stimuli to trigger shape changes [28]. However, these bistable structures often require attaching a shape memory polymer or an auxiliar structure to trigger the bistable structure, which has a limiting effect on the direction of loading and slows down the response. In this study, we use the concept of transition between

monostability and bistability to introduce a thermally bistable unit cell. We present a strategy to reconfigure a bistable state without requiring any inherent shape memory properties, nor any shape memory programming. Our design does not need any external element as a lever or muscle to trigger the geometry restoration. Furthermore, we may customize the design for any polymeric material and it only relies on the thermal softening of polymers, which is ubiquitous among most polymers [32]. The programmability is possible through varying geometrical features (i.e. struts‘ thickness and the width ratio of stiff material), which can be readily handled by AM. The shape memory effect in special alloys and polymers occurs when a temperature-induced phase transformation reverses deformation [33]. **Figure 1**a presents a typical cycle of load-deformation-temperature in shape memory alloys where a deformed detwinned martensite microstructure restores its original shape after being heated and transformed to the austenite phase. Controllable active deformation makes shape memory polymers (SMPs) and shape memory alloys (SMAs) capable of reconfiguring their shape by programming their response [33]. As a result, they have been implemented in a variety of applications from aerospace [34-37] and biomedical devices [38-41] to flexible electronics [42-46] and soft robotics [47-49].

The strategy we propose in this study helps to reproduce the shape memory effect (SME) without relying on the intrinsic memory effect in material and only by harnessing the bistability of a structure and thermal softening of polymeric materials. This strategy offers the customization of the shape memory effect in alternative polymeric materials or any other materials whose elastic modulus decreases with temperature. Subsequently, the current material selection limitations around shape-memory materials can be overcome, allowing a wide range of thermoplastic polymers to demonstrate shape memory behavior. AM enables us to modify simple parameters in the micro/mesoarchitectural design in order to customize the shape of the bistable structure so that we can achieve complex configurations and topologies that are not possible to fabricate with conventional SMA and SMP manufacturing techniques. Another major improvement we can achieve through thermally bistable structures is the rapid transition

between different stable phases by changing temperature. The shape restoration in SMAs and SMPs occurs through a gradual process [33] but the thermally bistable structure restores its original configuration swiftly through a snap-through behavior, which makes it appropriate for applications as an actuator.

Figure 1b shows the load-displacement-temperature curve of our developed bistable multi-material structure resembling that of SMAs. When we apply a compressive load of a certain value and then remove the load, the structure retains its deformed stable configuration. Then, the structure restores its original shape as soon as its temperature surpasses a critical value. In Figure 1b, we indicate the area under the curve when the force value is negative as "Bistability Energy (U_{bs})". This parameter is utilized as an index that determines whether a structure is bistable or not, i.e., a structure is bistable if and only if U_{bs} is non-zero. The bistable element that we use in our study is a fixed-guided tilted beam, which has been the subject of various studies for its bistability and negative stiffness behavior [8, 50, 51]. We form our unit cell by a pair of tilted beams connected to walls with tunable stiffness on both sides. A schematic view of the unit cell of this bistable structure is shown in Figure 1c, in which the bimaterial walls on each end of the struts have variable stiffness depending on the material composition, geometry, and temperature. The bottom part of the structure is considered fully clamped. Images (i) to (iv) in Figure 1d show the as-built structures at four different states; when the compressive force is applied (image ii) and removed (image iii), and when the structure is subjected to a temperature increase (image iv), which restores the original configuration (image i). The constituent material for the snapping bistable element is thermoplastic polyurethane (TPU) while the stiffer wall material is carbon-fiber-reinforced (CFR) Nylon. The properties of both materials at room temperature are reported in **Table A1** in the **Appendix A**.

2. Results and Discussion

We resort to finite element (FE) simulation and experimentation to investigate different design parameters and their effects on the responses of thermally bistable structures. FE simulations

have been conducted using the transient structural module of commercial ANSYS software version 2021R1. Unit cells are analyzed based on the nonlinear two-dimensional (2D) plane strain theory and each cell is discretized with approximately 50,000 elements. Three-node linear triangular element geometry with Nodal Based Strain (NBS) formulation is selected as the element type for modeling the structure. A rigid body is attached to the top of the lattice structures to apply the deformation-driven loading on each cell, while the bottom part of the body is fully fixed. Element and body self-contact effects are taken into account by defining frictional contact between different parts of each unit cell. The friction coefficients between body and rigid parts and body self-contact are set to be 0.1. Details of experiments and sample fabrication are presented in the **Appendix A**.

In **Figure 2**a, we present the FE results for the effect of changing different design parameters on the force-displacement curves of the mechanically bistable unit cell made of one material. We find that increasing the number of struts (n), strut angle (θ), or strut thickness (t) leads to higher absolute values of maximum force, when the strut length, $L = 50\text{mm}$, $w = 10\text{mm}$, and $D = 20\text{mm}$ are held constant. Taking a closer look at Figure 2a shows that stiffer walls lead to higher bistability energy. Subsequently, in Figure 2b, the bistability energy is plotted for the same structure with $\theta = 40°$ and $H/D = 3$ while w, varies, that demonstrates the bistability energy increases when the wall becomes thicker and stiffer.

We present a new approach to customize the force-displacement curves by adding a ribbon of stiffer material on each side of the wall and without changing the total size of the 1D unit cell. Figure 2c presents the force-displacement curves for unit cells with different relative widths of a stiff material (w_{st}/w). It demonstrates this ribbon of stiff material can have a critical effect on the force-displacement curve and the bistability energy. A higher value of the relative width of the stiff material (w_{st}/w) increases the absolute value of the maximum and minimum reaction forces, and consequently, the bistability energy increases. Figure 2d reiterates the effect

of the stiffer material on the changes in the bistability energy of unit cells for alternative strut thicknesses and angles. In particular, we can see that in the structures with thicker struts, the presence of a stiff ribbon material on the sides can transform a monostable structure to a bistable structure with relatively large bistability energy.

We propose a strategy to accumulate the effect of different parameters affecting the wall stiffness by introducing a non-dimensional equivalent wall stiffness parameter (K_{eq}) to study the effect of wall stiffness on the bistability of a unit cell. The rationality and formulation for defining this parameter are explained in the **Appendix B**. **Figure 3**a shows that the equivalent stiffness parameter, K_{eq}, increases uniformly by increasing the relative width of a stiffer material in the wall of unit cells. Plotting the non-dimensional bistability energy versus the equivalent wall stiffness parameter for unit cells with $n = 2$, $\theta = 40°$, and $H/D = 3$ shows there is a threshold value for the equivalent wall stiffness parameter depending on the strut thickness (Figure 3b). In another word, a structure is not bistable unless its equivalent wall stiffness is higher than a threshold value mainly determined by the strut thickness and angle. Figure 3b also shows that the bistability energy increases rapidly for a limited range when the equivalent wall stiffness goes beyond the threshold value and after that, the bistability is almost independent of the wall stiffness. In Figure 3c-d, phase diagrams are presented for the same unit cells for three different strut angles, where the equivalent wall stiffness, K_{eq}, is plotted versus the strut thickness. Designs above the plotted lines represent unit cells that are mechanically bistable while a structure whose wall stiffness is lower than that of threshold is monostable. We can observe that the threshold wall stiffness parameter increases with the strut thickness for all three strut angles presented in Figures 3c-d. Comparing the three graphs, one may conclude that the threshold wall stiffness is generally decreasing for unit cells with higher strut angles.

The correlation between the wall stiffness and bistability of the structure enables controlling the response of a snapping unit cell without changing the overall dimensions of the structure. Here, we take advantage of this possibility to program the thermal response of the structure and the temperature at which the restoration is triggered (*Triggering Temperature*); consequently, two materials with distinctive stiffness versus temperature properties are used for the fabrication of the wall. Dynamic Mechanical Analysis (DMA) of elastic moduli of these two polymers are presented in **Appendix C**. By attaching two different materials for the walls, we can tune the wall stiffness in a way that a mechanical bistable structure becomes thermally bistable, i.e., restore its original shape by heating. **Figure 4**a presents a force-displacement-temperature diagram for structures with different stability conditions. Based on this definition, a mechanically bistable structure can be either thermally bistable or monostable, while a mechanically monostable structure is essentially thermally monostable. Figures 4b and 4c depict force-displacement temperature for unit cells with various strut thicknesses at two different angles, which are mechanically and thermally bistable structures. Unlike shape memory alloys and polymers, a thermally bistable structure restores its initial configuration swiftly at a specific temperature, i.e., the triggering temperature. Figure 4 shows that the triggering temperature has an inverse relationship with strut thickness, meaning that a mechanically bistable structure with higher strut thickness has a lower triggering temperature. As illustrated in **Appendix D**, the effect of thermal expansion on this behavior is negligible based on our conducted FE results; the triggering temperature does not change significantly even if the coefficient of thermal expansion (CTE) changes in a relatively large range ($10^{-6} - 10^{-4}\ ^{\circ}\mathrm{C}^{-1}$).

The colormap in **Figure 5**a presents the triggering temperatures for different unit cell designs with a 40° strut angle. We observe that the highest triggering temperature belongs to the structures with the minimum strut thickness, while a structure with thicker struts may be mechanically or thermally monostable depending on their wall stiffnesses (K_{eq}). Figure 5a also

shows that although the structures with thicker struts lead to higher bistability energy and more stable deformed configuration (Figure 2a), their triggering temperature is often lower than unit cells with thinner struts. Plotting the triggering temperature versus trapped energy in Figure 5b confirms that there is an inverse correlation between the bistability energy and triggering temperature.

Figures 5c-d present the force-displacement curves for eight different designs obtained by finite element simulations and experimental tests. Comparing FE and experimental data shows that the numerical simulation generally overestimates the absolute value of the force compared to the experimental data, while they both predict the same trend for the effect of different design parameters. A similar conclusion can be drawn for triggering temperatures; the experimental values are predominantly lower than FE predictions although the general behavior is comparable with FE predictions (Figure 5e). The slight deviation between FE and experimental results generally stems from the presence of defects in 3D printing as it is challenging to fabricate perfectly symmetric samples as the travel path of the extruder cannot be identical when printing each side. Non-uniform extrusion may also lead to inconsistency in the thickness along the struts. The thickness variation together with possible misalignment during the mechanical test results in unsymmetric deformation of the as-built 3D printed structures and subsequently the results deviate from the numerical results of ANSYS developed based on as-designed structures. Further information about the manufacturing defects is presented in **Appendix E**.

In **Figure 6**, we illustrate the possibility of transforming a bistable structure into a monostable one by changing temperature. The monostable structure shows an elastic behavior even during large deformations; a behavior that resembles the superelasticity of SMA when they reach the temperature of the Austenite Phase. Figures 6a-b demonstrate the mechanical and thermal loading sequences together with snapshots during the experiment and FE simulation of a thermally bistable structure. In Figure 6a, the unit cell is deformed mechanically, and the

structure remains in the stable deformed configuration even after the load is removed. When we increase the temperature of the structure, the unit cell restores its original shape. In Figure 6b, the sequence of thermal and mechanical loading is reversed, i.e., we increase the temperature of the whole structure prior to deformation. This loading sequence results in a drop in the equivalent wall stiffness, and consequently, a thermally bistable structure becomes mechanically monostable. In this case, both experimental tests and FE analyses show that the structure will restore its original shape as soon as the mechanical loading is removed. We can see that FE simulations and experiments suggest similar behavior and deformation patterns but the deformed configurations predicted by FE analysis are more symmetric because the structure is as-designed and the loading is considered perfectly symmetric. The stress contours of the same structure at two different configurations and temperature in **Figure F1** shows that when the temperature increases, the walls become more flexible and their equivalent stress drastically decreases. However, the stress at the struts depends more on the deformed configuration and less on the temperature. The experimental results for a sequence of loading and unloading is presented in **Appendix G** and the videos of these experiments together with loading sequences are presented in the **Supplementary Movies S1** and **S2**.

In **Figures 7**a and b, we investigate the possibility of tesselating the proposed structure through FE analysis. Figure 7a presents the architecture with hierarchical tesselation of the design motif, introduced in Figure 1, in the vertical direction. The force-displacement diagram shows that the structure undergoes a series of snap-through behavior in a sequence starting from the smallest unit cell in the structure because the smallest unit cell reconfigures with a lower value of load. We observe a similar behavior when the temperature is increased. i.e., the smallest to largest unit cell restores its original shape and by a further increase in temperature, the middle and the largest cells restore their shapes, respectively. Horizontal tesselation is another strategy to put thermally bistable unit cells together and develop a one-dimensional metamaterial as presented in Figure 7b. In this one-dimensional mechanical metamaterial, the force-displacement curve is

similar to that of a single design motif; however, the temperature-displacement curve is different. When temperature increases, the cell whose stiff part (w_{st}/w), is the smallest compared to the other cells, restores first and it also excites the other two cells to reconfigure. Generally, these tessellation strategies show that depending on the application we can customize the response of thermally bistable structure by amplifying the deformation or tailoring the triggering temperature.

3. Conclusions

The proposed design paradigm enables attaining shape memory behavior without exploiting special polymers or alloys with inherent shape memory properties and without the required SME programming. Our study indicates that the bistability behavior of a snapping unit cell significantly depends on its boundary conditions, i.e., surrounding walls; stiffening the wall can transform a monostable structure to a bistable one, and vice versa. Therefore, we design a bistable unit cell with bimaterial walls in order to control wall stiffness by changing the combination of the constituent materials of the walls. The thermal softening nature of polymeric walls' materials enables us to control the bistability behavior of the structure by changing temperature. The resulting structure is thermally bistable; a structure that can have two distinctive configurations by changing temperature. The triggering temperature of the structure can be controlled and programmed by changing the dimensions and the ratio of properties of constituent materials.

The main advantage of the proposed design is enabling the utilization of a wider range of materials for the shape memory effect. Inducing a relatively large deformation to a body by changing temperature has so far been observed mainly in SMPs and SMAs but the proposed design paradigm offers to generate the same response for any polymers whose elastic moduli change with temperature. Furthermore, the response of SMPs and SMAs to temperature is

gradual while the proposed thermally bistable structure can transform to different stable states in a sudden snapping behavior. This behavior paves the path for the utilization of thermal bistability for self-sensing actuators since the introduced bistable bimaterial structure quickly responds at the triggering temperature.

Acknowledgments

Authors acknowledge the financial support by Natural Sciences and Engineering Research Council of Canada through NSERC Discovery Grants to A.H.Akbarzadeh, S. Bodkhe, and D.Therriault. In addition, A.H.Akbarzadeh acknowledges partial financial support from the Canada Research Chairs program. H. Niknam is supported by Quebec Research Fund - Nature and Technologies (FRQNT) post-doctoral awards (B3X). This research was enabled in part by support provided by CalculQuebec and Compute Canada. The contribution of Hossein Mofatteh at AM^3L laboratory of McGill University in the 3D printing process is also acknowledged.

Received: ((will be filled in by the editorial staff))
Revised: ((will be filled in by the editorial staff))
Published online: ((will be filled in by the editorial staff))

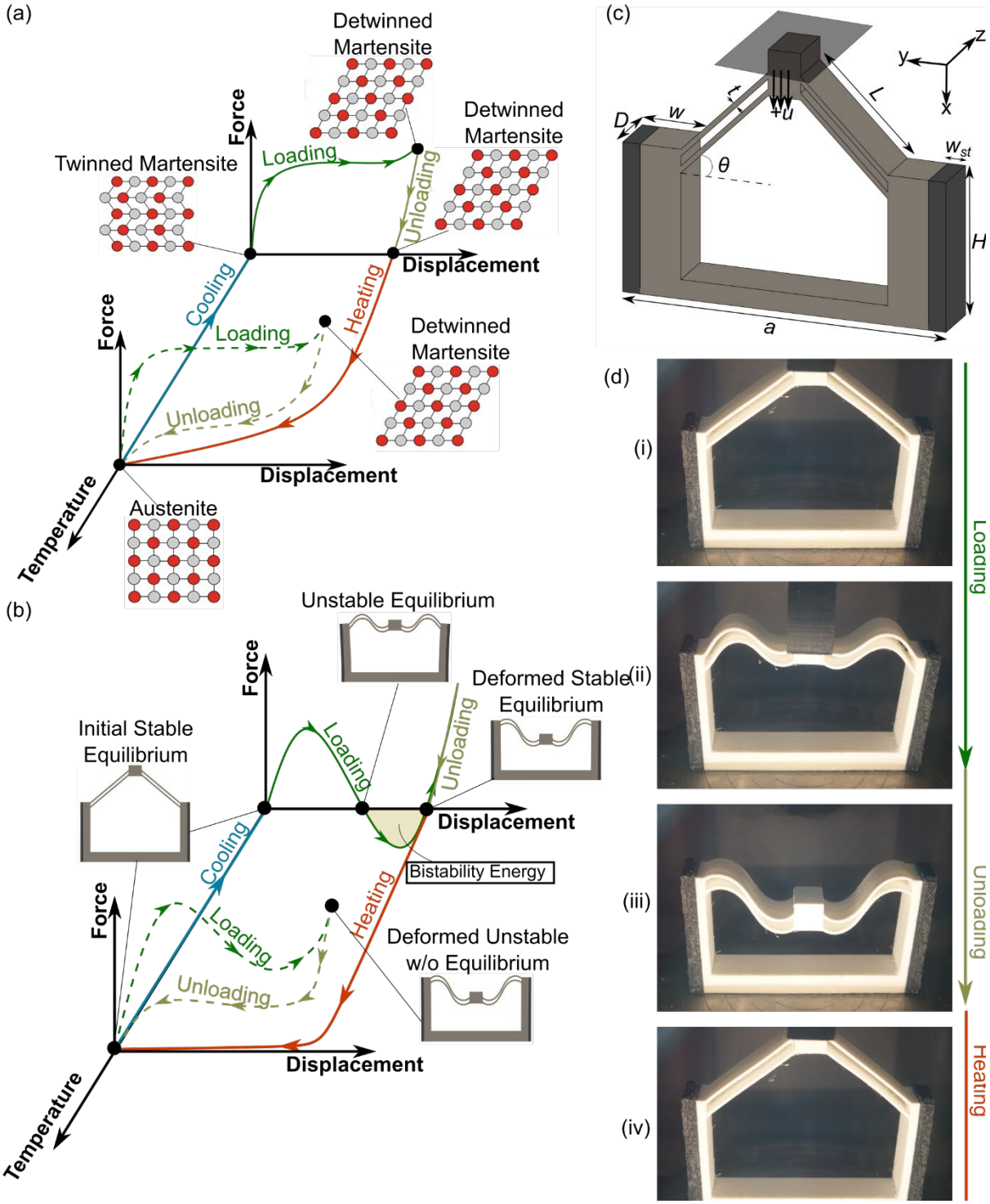

Figure 1. (a) Force-displacement-temperature curves for a shape memory alloy with the microstructure conditions at different states. (b) Force-displacement-temperature curves for a thermally bi-stable structure at different states. (c) Schematic view of the designed motif. (d) Images of the 3D printed bimaterial bistable structure during loading, unloading, and heating

((i) First stable equilibrium, (ii) Unstable equilibrium, (iii), Second/Deformed stable equilibrium, (iv) First stable equilibrium).

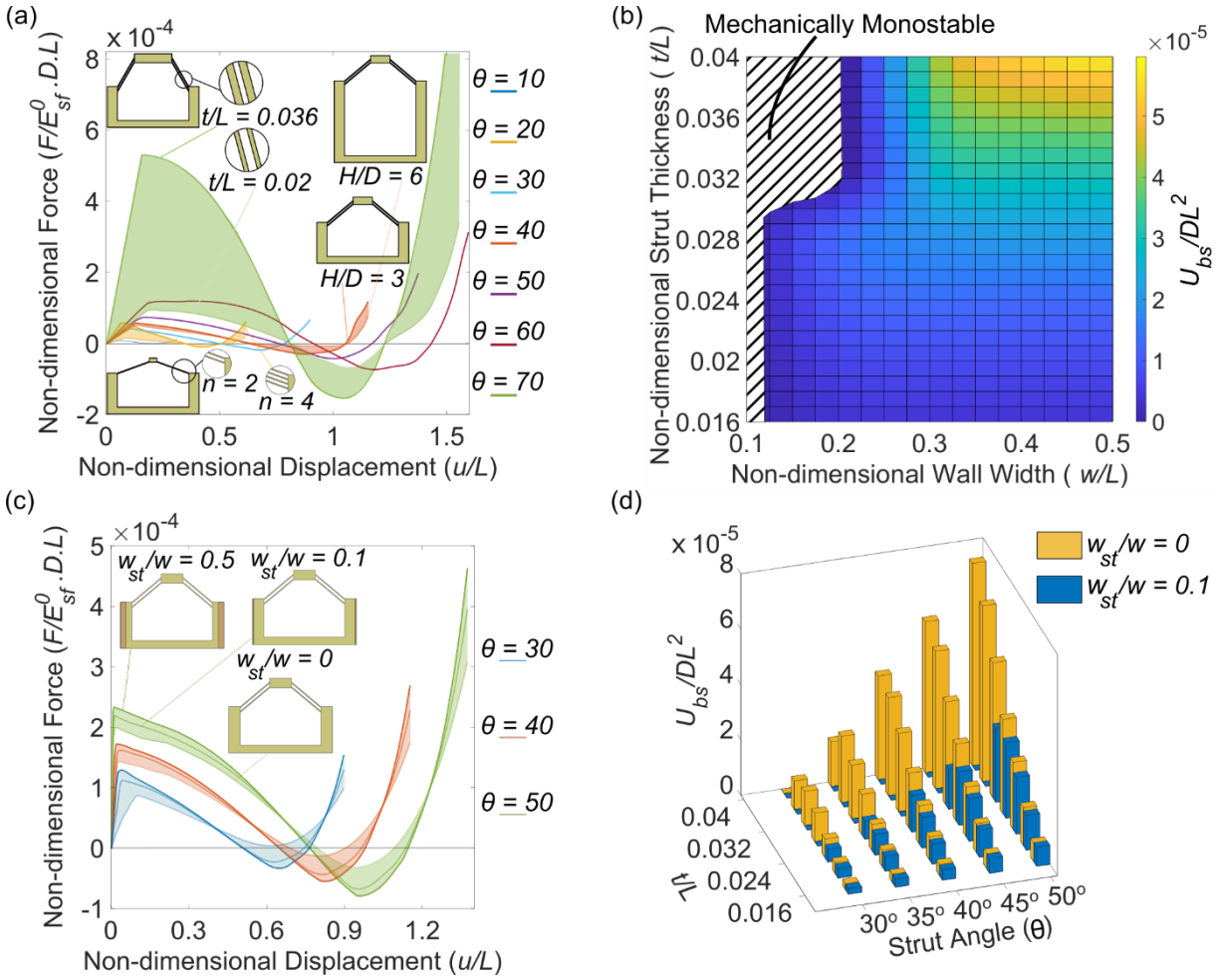

Figure 2. (a) The effect of different geometric design parameters on the snap-through behavior of the single-materials bistable structure. (b) The effect of wall width (w/L) on the bistability energy for the single-material unit cell. (c) Force-displacement curves of snap-through behavior of the bimaterial unit cell with a different strut thickness of a stiff material attached to the soft walls. (d) Bistability energy of unit cells with different strut thickness and angles with and without stiff material attached to the walls.

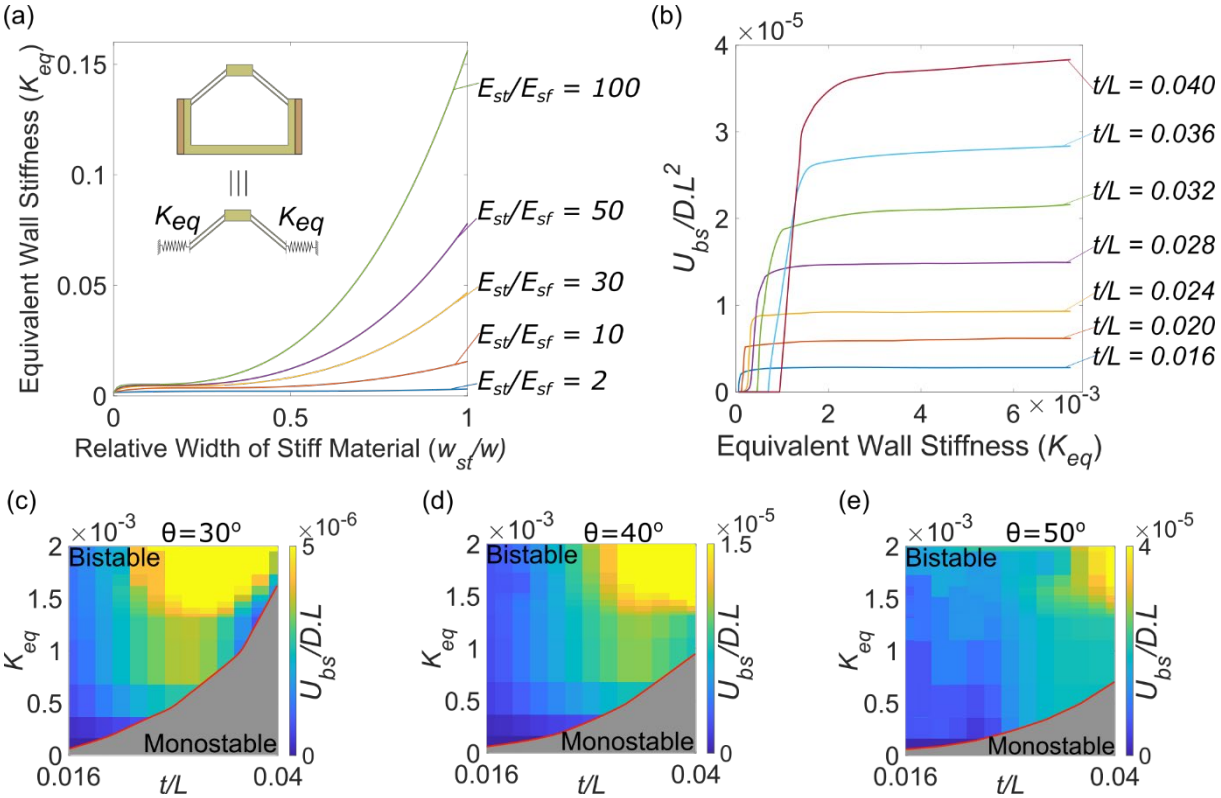

Figure 3. (a) Variation of equivalent wall stiffness (K_{eq}) for different constituent materials. (b) Non-dimensional bistability energy versus equivalent wall stiffness parameter for unit cells with different strut thickness. (c), (d), (e) Phase diagrams showing the variation of threshold wall stiffness versus thickness for different struts angles $\theta = 30°$, $\theta = 40°$, and $\theta = 50°$.

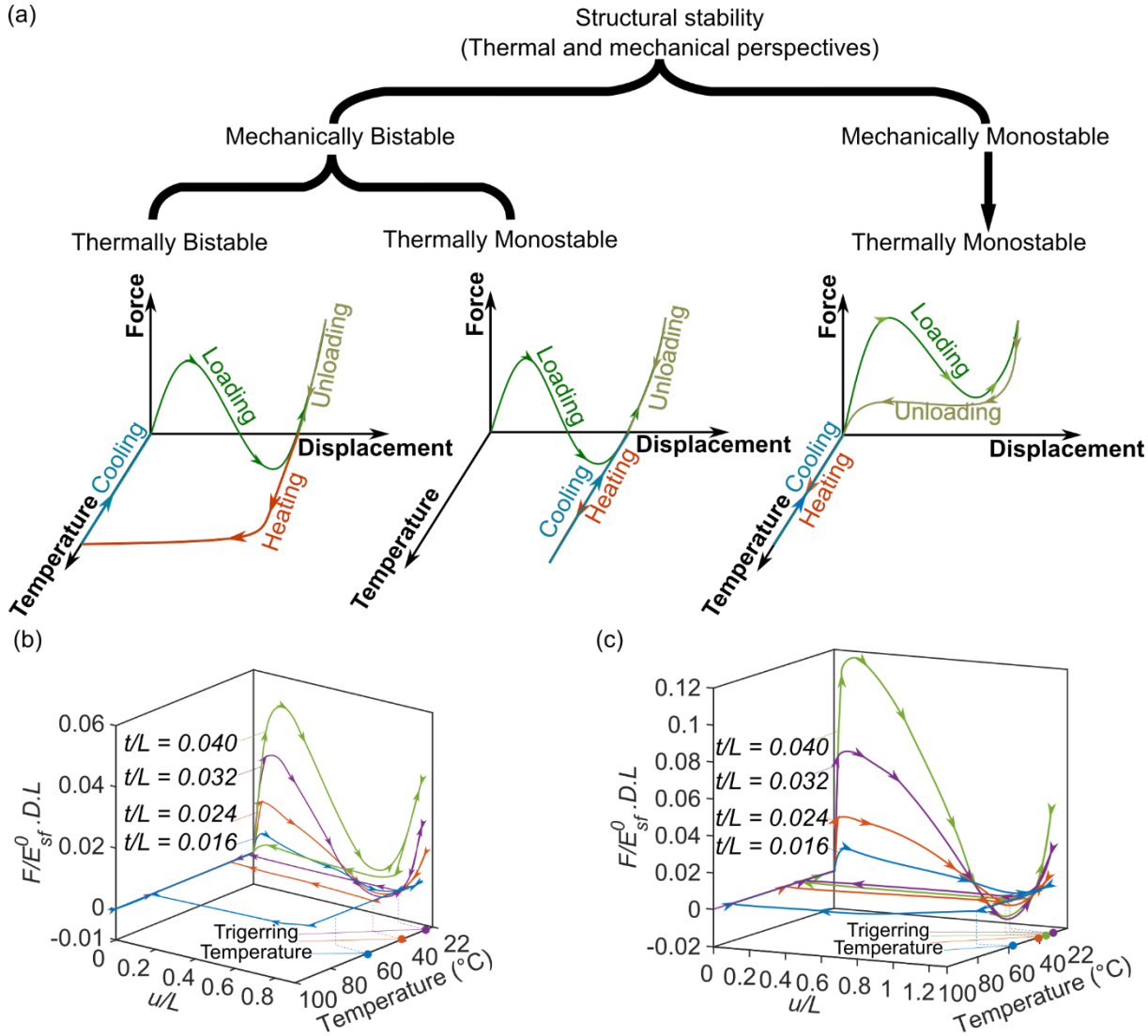

Figure 4. (a) Force-displacement-temperature curves for different structures from thermal and mechanical stability perspectives. Force – displacement – temperature response for unit cells with different thickness and strut angles of for strut angles (b) $\theta = 30°$ and (c) $\theta = 50°$.

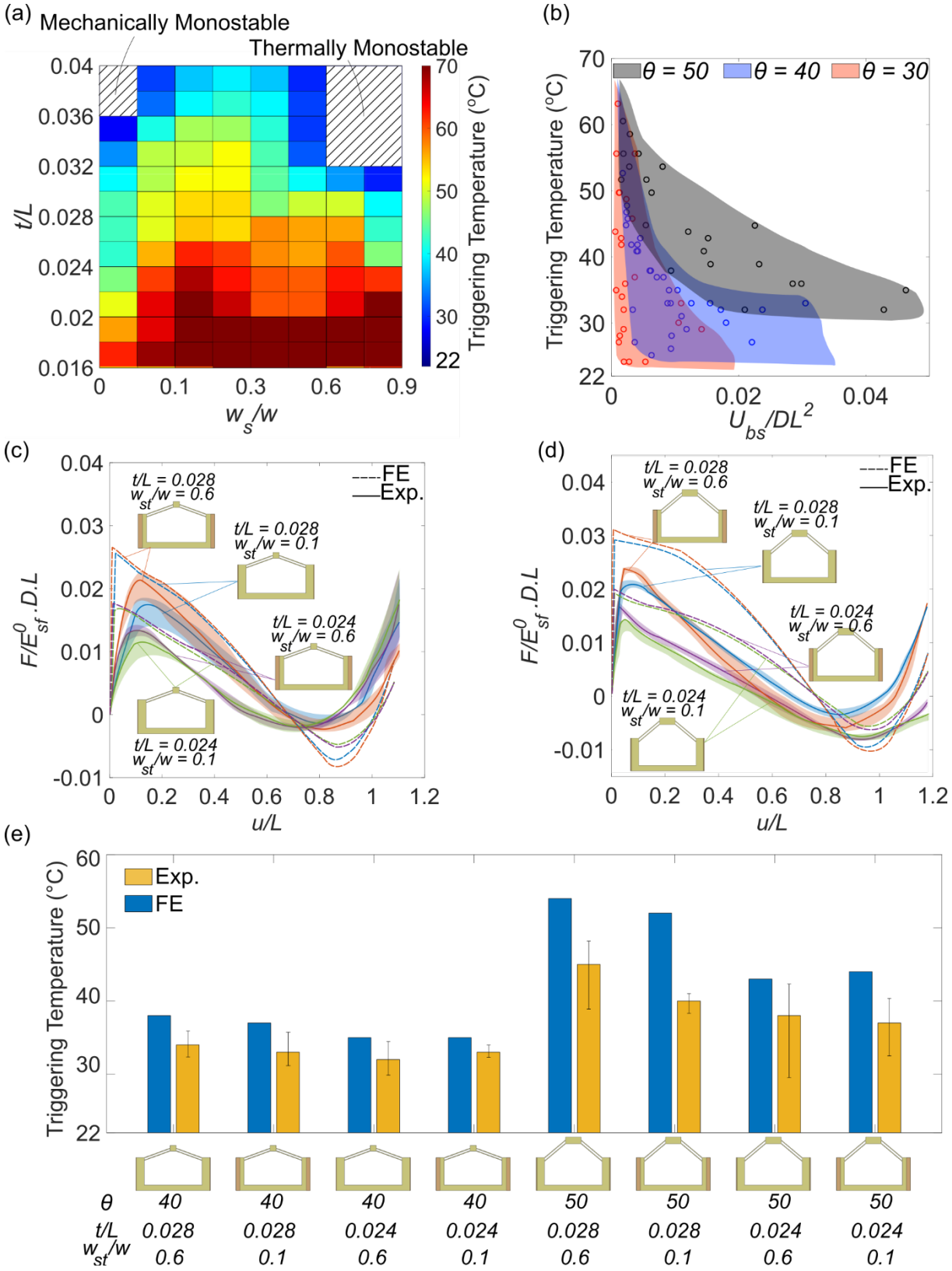

Figure 5. (a) Triggering temperature for unit cells with different strut thicknesses and stiff material on the wall for strut angle $\theta = 40°$. (b) The effect of non-dimensional bistability energy on triggering temperature for different geometries. Comparison of force-displacement

curves obtained from FE and experiments for strut angles (c) $\theta = 30°C$ and, (d) $\theta = 50°C$. (e) Comparison of triggering temperatures obtained from FE and experiments.

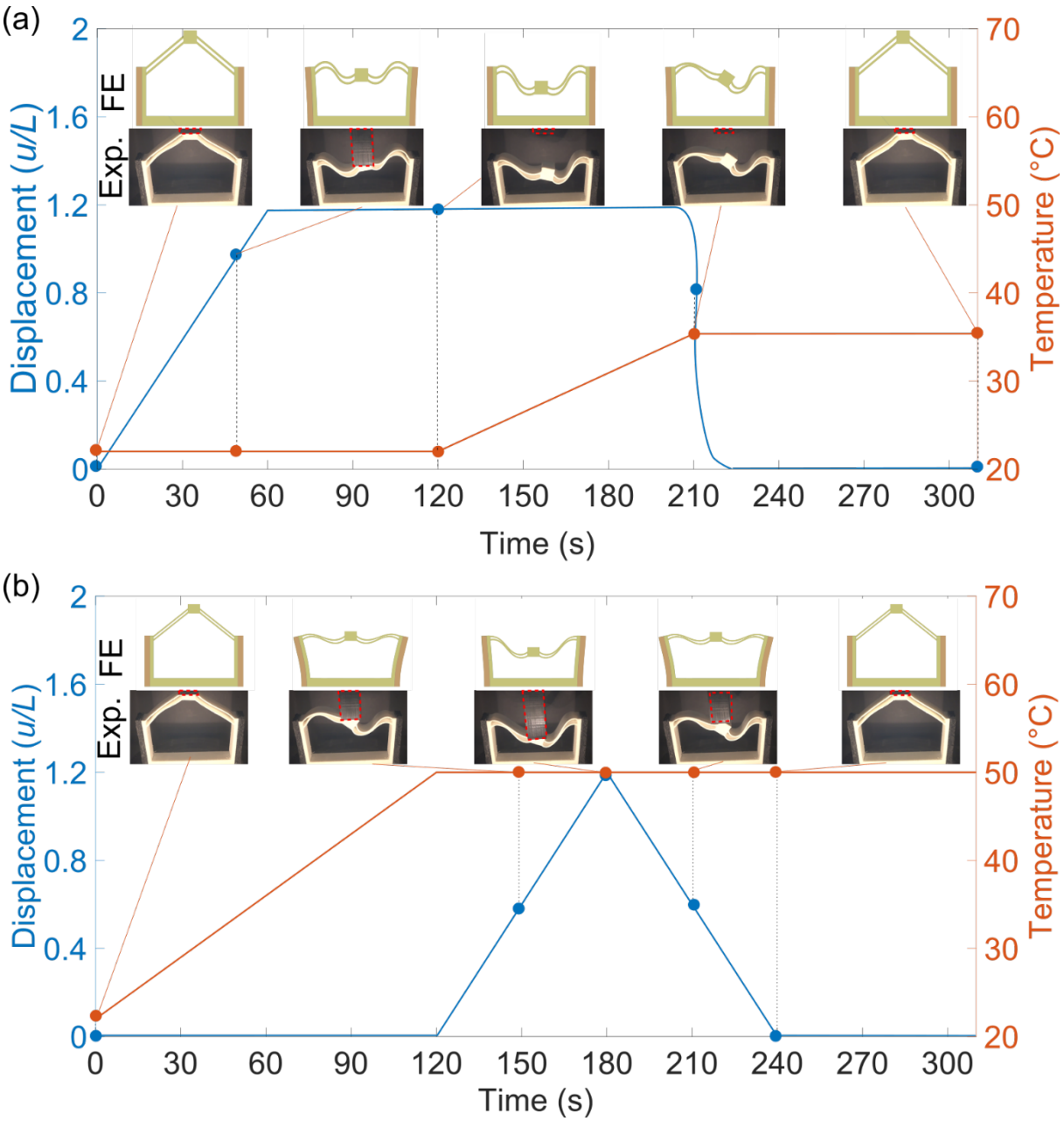

Figure 6. (a) and (b) Displacement – time response and snapshots of FE and experimental analyses for a 1D unit cell with $\theta = 50°C$, $w_{st}/w = 0.6$, and $t/L = 0.028$ with two different loading sequences.

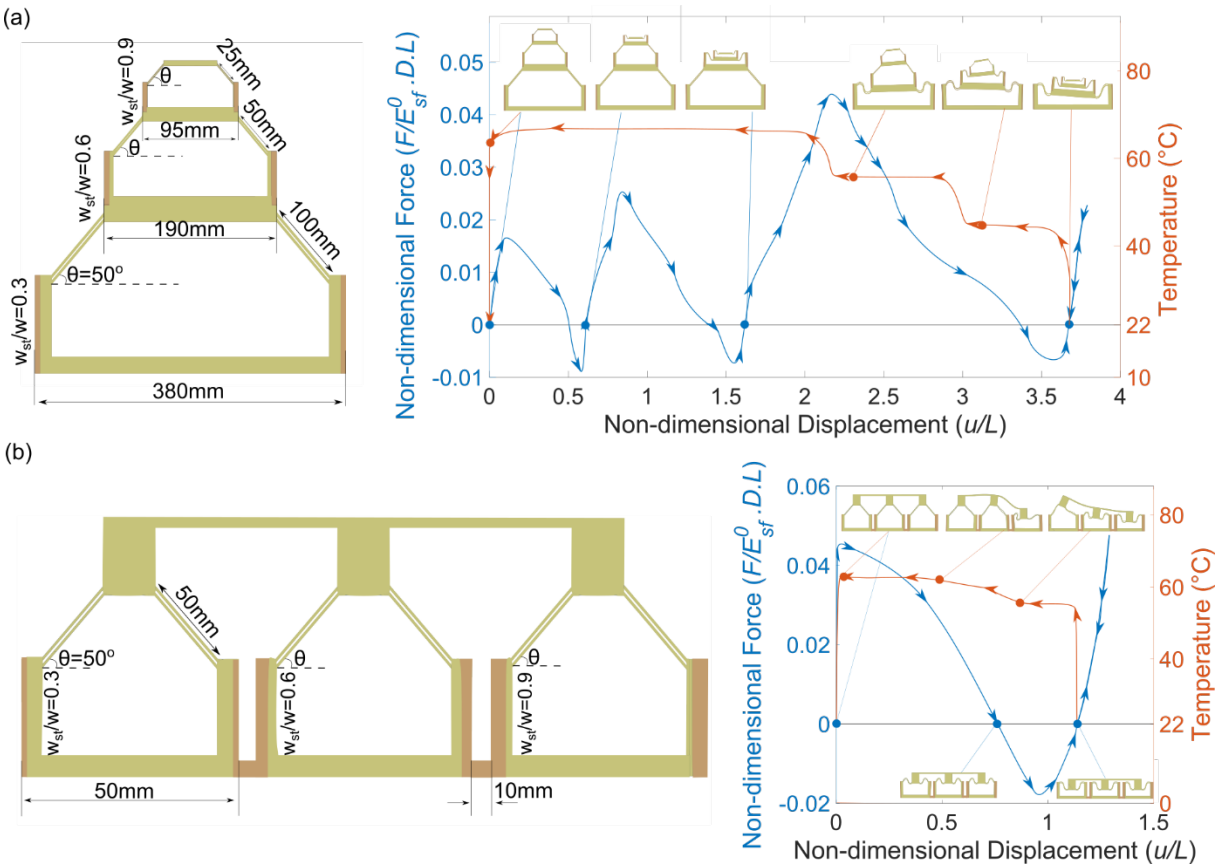

Figure 7. (a) Force-displacement and temperature-displacement diagrams for a hierarchically tesselated thermally bistable structure with $\theta = 40°$ and $t/L = 0.028$. (b) Force-displacement and temperature-displacement diagrams for horizontal and heterogenous tesselation of thermally bistable structures with $\theta = 40°$,$t/L = 0.028$, and alternative w_{st}/w .

References

[1] P. Rothemund, A. Ainla, L. Belding, D.J. Preston, S. Kurihara, Z. Suo, G.M. Whitesides, A soft, bistable valve for autonomous control of soft actuators, Science Robotics 3(16) (2018) eaar7986.

[2] D. Melancon, B. Gorissen, C.J. García-Mora, C. Hoberman, K. Bertoldi, Multistable inflatable origami structures at the metre scale, Nature 592(7855) (2021) 545-550.

[3] S. Mhatre, E. Boatti, D. Melancon, A. Zareei, M. Dupont, M. Bechthold, K. Bertoldi, Deployable Structures Based on Buckling of Curved Beams Upon a Rotational Input, Advanced Functional Materials n/a(n/a) (2021) 2101144.

[4] H. Shao, S. Wei, X. Jiang, D.P. Holmes, T.K. Ghosh, Bioinspired Electrically Activated Soft Bistable Actuators, Advanced Functional Materials 28(35) (2018) 1802999.

[5] J. Zhang, K. Yang, R. Li, A bistable nonlinear electromagnetic actuator with elastic boundary for actuation performance improvement, Nonlinear Dynamics 100(4) (2020) 3575-3596.

[6] J. Shi, H. Mofatteh, A. Mirabolghasemi, G. Desharnais, A. Akbarzadeh, Programmable Multistable Perforated Shellular, Advanced Materials 33(42) (2021) 2170328.

[7] T. Frenzel, C. Findeisen, M. Kadic, P. Gumbsch, M. Wegener, Tailored Buckling Microlattices as Reusable Light-Weight Shock Absorbers, Advanced Materials 28(28) (2016) 5865-5870.

[8] S. Shan, S.H. Kang, J.R. Raney, P. Wang, L. Fang, F. Candido, J.A. Lewis, K. Bertoldi, Multistable Architected Materials for Trapping Elastic Strain Energy, Advanced Materials 27(29) (2015) 4296-4301.

[9] H.Y. Jeong, S.-C. An, I.C. Seo, E. Lee, S. Ha, N. Kim, Y.C. Jun, 3D printing of twisting and rotational bistable structures with tuning elements, Scientific Reports 9(1) (2019) 324.

[10] H.Y. Jeong, E. Lee, S. Ha, N. Kim, Y.C. Jun, Multistable Thermal Actuators Via Multimaterial 4D Printing, Advanced Materials Technologies 4(3) (2019) 1800495.

[11] T. Chen, K. Shea, Design and Fabrication of Hierarchical Multi-Stable Structures Through Multi-Material Additive Manufacturing, 2016.

[12] K. Bertoldi, Harnessing Instabilities to Design Tunable Architected Cellular Materials, Annual Review of Materials Research 47(1) (2017) 51-61.

[13] A. Pal, V. Restrepo, D. Goswami, R.V. Martinez, Exploiting Mechanical Instabilities in Soft Robotics: Control, Sensing, and Actuation, Advanced Materials 33(19) (2021) 2006939.

[14] O. Peretz, A.K. Mishra, R.F. Shepherd, A.D. Gat, Underactuated fluidic control of a continuous multistable membrane, Proceedings of the National Academy of Sciences 117(10) (2020) 5217.

[15] V. Ramachandran, M.D. Bartlett, J. Wissman, C. Majidi, Elastic instabilities of a ferroelastomer beam for soft reconfigurable electronics, Extreme Mechanics Letters 9 (2016) 282-290.

[16] D.P. Holmes, B. Tavakol, G. Froehlicher, H.A. Stone, Control and manipulation of microfluidic flow via elastic deformations, Soft Matter 9(29) (2013) 7049-7053.

[17] B. Yang, B. Wang, W.K. Schomburg, A thermopneumatically actuated bistable microvalve, Journal of Micromechanics and Microengineering 20(9) (2010) 095024.

[18] K. Luo, P. Rothemund, G.M. Whitesides, Z. Suo, Soft kink valves, Journal of the Mechanics and Physics of Solids 131 (2019) 230-239.

[19] D.J. Preston, H.J. Jiang, V. Sanchez, P. Rothemund, J. Rawson, M.P. Nemitz, W.-K. Lee, Z. Suo, C.J. Walsh, G.M. Whitesides, A soft ring oscillator, Science Robotics 4(31) (2019) eaaw5496.

[20] E. Ben-Haim, L. Salem, Y. Or, A.D. Gat, Single-Input Control of Multiple Fluid-Driven Elastic Actuators via Interaction Between Bistability and Viscosity, Soft Robotics 7(2) (2019) 259-265.

[21] O.R. Bilal, A. Foehr, C. Daraio, Bistable metamaterial for switching and cascading elastic vibrations, Proc Natl Acad Sci U S A 114(18) (2017) 4603-4606.
[22] H. Fu, K. Nan, W. Bai, W. Huang, K. Bai, L. Lu, C. Zhou, Y. Liu, F. Liu, J. Wang, M. Han, Z. Yan, H. Luan, Y. Zhang, Y. Zhang, J. Zhao, X. Cheng, M. Li, J.W. Lee, Y. Liu, D. Fang, X. Li, Y. Huang, Y. Zhang, J.A. Rogers, Morphable 3D mesostructures and microelectronic devices by multistable buckling mechanics, Nature Materials 17(3) (2018) 268-276.
[23] Y. Kim, H. Yuk, R. Zhao, S.A. Chester, X. Zhao, Printing ferromagnetic domains for untethered fast-transforming soft materials, Nature 558(7709) (2018) 274-279.
[24] T. Chen, M. Pauly, P.M. Reis, A reprogrammable mechanical metamaterial with stable memory, Nature 589(7842) (2021) 386-390.
[25] N. Nadkarni, A.F. Arrieta, C. Chong, D.M. Kochmann, C. Daraio, Unidirectional Transition Waves in Bistable Lattices, Physical Review Letters 116(24) (2016) 244501.
[26] T. Chen, O.R. Bilal, K. Shea, C. Daraio, Harnessing bistability for directional propulsion of soft, untethered robots, Proceedings of the National Academy of Sciences 115(22) (2018) 5698.
[27] K. Che, C. Yuan, H.J. Qi, J. Meaud, Viscoelastic multistable architected materials with temperature-dependent snapping sequence, Soft matter 14(13) (2018) 2492-2499.
[28] Y. Jiang, L.M. Korpas, J.R. Raney, Bifurcation-based embodied logic and autonomous actuation, Nature Communications 10(1) (2019) 128.
[29] Y. Zhang, M. Velay-Lizancos, D. Restrepo, N.D. Mankame, P.D. Zavattieri, Architected material analogs for shape memory alloys, Matter 4(6) (2021) 1990-2012.
[30] L.-C. Wang, W.-L. Song, Y.-J. Zhang, M.-J. Qu, Z. Zhao, M. Chen, Y. Yang, H. Chen, D. Fang, Active Reconfigurable Tristable Square-Twist Origami, Advanced Functional Materials 30(13) (2020) 1909087.
[31] L.C. Wang, W.L. Song, D. Fang, Twistable Origami and Kirigami: from Structure-Guided Smartness to Mechanical Energy Storage, ACS applied materials & interfaces 11(3) (2019) 3450-3458.
[32] K. Chen, K.S. Schweizer, Theory of Yielding, Strain Softening, and Steady Plastic Flow in Polymer Glasses under Constant Strain Rate Deformation, Macromolecules 44(10) (2011) 3988-4000.
[33] Y. Xia, Y. He, F. Zhang, Y. Liu, J. Leng, A Review of Shape Memory Polymers and Composites: Mechanisms, Materials, and Applications, Advanced Materials 33(6) (2021) 2000713.
[34] Y. Liu, H. Du, L. Liu, J. Leng, Shape memory polymers and their composites in aerospace applications: a review, Smart Materials and Structures 23(2) (2014) 023001.
[35] F. Li, Y. Liu, J. Leng, Progress of shape memory polymers and their composites in aerospace applications, Smart Materials and Structures 28(10) (2019) 103003.
[36] T. Chen, O.R. Bilal, R. Lang, C. Daraio, K. Shea, Autonomous Deployment of a Solar Panel Using Elastic Origami and Distributed Shape-Memory-Polymer Actuators, Physical Review Applied 11(6) (2019) 064069.
[37] V.L. Le, V.T. Le, N.S. Goo, Deployment performance of shape memory polymer composite hinges at low temperature, Journal of Intelligent Material Systems and Structures 30(17) (2019) 2625-2638.
[38] A. Lendlein, R. Langer, Biodegradable, Elastic Shape-Memory Polymers for Potential Biomedical Applications, Science 296(5573) (2002) 1673.
[39] J. Ortega, D. Maitland, T. Wilson, W. Tsai, Ö. Savaş, D. Saloner, Vascular Dynamics of a Shape Memory Polymer Foam Aneurysm Treatment Technique, Annals of Biomedical Engineering 35(11) (2007) 1870-1884.
[40] S.M. Herting, Y. Ding, A.J. Boyle, D. Dai, L.D. Nash, S. Asnafi, D.R. Jakaitis, C.R. Johnson, L.M. Graul, C. Yeh, D.F. Kallmes, R. Kadirvel, D.J. Maitland, In vivo comparison

of shape memory polymer foam-coated and bare metal coils for aneurysm occlusion in the rabbit elastase model, Journal of Biomedical Materials Research Part B: Applied Biomaterials 107(8) (2019) 2466-2475.
[41] A. Melocchi, M. Uboldi, N. Inverardi, F. Briatico-Vangosa, F. Baldi, S. Pandini, G. Scalet, F. Auricchio, M. Cerea, A. Foppoli, A. Maroni, L. Zema, A. Gazzaniga, Expandable drug delivery system for gastric retention based on shape memory polymers: Development via 4D printing and extrusion, International Journal of Pharmaceutics 571 (2019) 118700.
[42] Z. Yu, X. Niu, Z. Liu, Q. Pei, Intrinsically Stretchable Polymer Light-Emitting Devices Using Carbon Nanotube-Polymer Composite Electrodes, Advanced Materials 23(34) (2011) 3989-3994.
[43] U. Adiyan, T. Larsen, J.J. Zárate, L.G. Villanueva, H. Shea, Shape memory polymer resonators as highly sensitive uncooled infrared detectors, Nature Communications 10(1) (2019) 4518.
[44] J. Wang, Q. Zhao, Y. Wang, Q. Zeng, T. Wu, X. Du, Self-Unfolding Flexible Microelectrode Arrays Based on Shape Memory Polymers, Advanced Materials Technologies 4(11) (2019) 1900566.
[45] R. Liu, X. Kuang, J. Deng, Y.-C. Wang, A.C. Wang, W. Ding, Y.-C. Lai, J. Chen, P. Wang, Z. Lin, H.J. Qi, B. Sun, Z.L. Wang, Shape Memory Polymers for Body Motion Energy Harvesting and Self-Powered Mechanosensing, Advanced Materials 30(8) (2018) 1705195.
[46] T. Ware, D. Simon, C. Liu, T. Musa, S. Vasudevan, A. Sloan, E.W. Keefer, R.L. Rennaker Ii, W. Voit, Thiol-ene/acrylate substrates for softening intracortical electrodes, Journal of Biomedical Materials Research Part B: Applied Biomaterials 102(1) (2014) 1-11.
[47] M. Yamada, M. Kondo, R. Miyasato, Y. Naka, J.-i. Mamiya, M. Kinoshita, A. Shishido, Y. Yu, C.J. Barrett, T. Ikeda, Photomobile polymer materials—various three-dimensional movements, Journal of Materials Chemistry 19(1) (2009) 60-62.
[48] C. Wang, K. Sim, J. Chen, H. Kim, Z. Rao, Y. Li, W. Chen, J. Song, R. Verduzco, C. Yu, Soft Ultrathin Electronics Innervated Adaptive Fully Soft Robots, Advanced Materials 30(13) (2018) 1706695.
[49] Y.-Y. Xiao, Z.-C. Jiang, X. Tong, Y. Zhao, Biomimetic Locomotion of Electrically Powered “Janus” Soft Robots Using a Liquid Crystal Polymer, Advanced Materials 31(36) (2019) 1903452.
[50] C. Findeisen, J. Hohe, M. Kadic, P. Gumbsch, Characteristics of mechanical metamaterials based on buckling elements, Journal of the Mechanics and Physics of Solids 102 (2017) 151-164.
[51] F. Ma, G. Chen, Bi-BCM: A Closed-Form Solution for Fixed-Guided Beams in Compliant Mechanisms, Journal of Mechanisms and Robotics 9(1) (2016).

Appendix A: Experimental details

Sample Preparation: Soft and stiff parts of the samples were fabricated by Ultimaker S3, a Fused Filament Fabrication (FFF) 3D printer. The soft parts were printed using a commercial Flexfill TPU 98A filament with a hundred percent infill and rectilinear pattern (-45º/45º lay-up), extrusion temperature of 220 ºC, bed temperature of 80 ºC, and 0.4 mm nozzle diameter. The stiff parts were printed out of commercial 3DXTech Gen3 CFR-Nylon with a hundred percent infill, extrusion temperature of 275ºC, bed temperature of 80ºC, and 0.6mm nozzle diameter. The properties of each material at room temperature are reported in **Table A1**.

Table A1. Properties of constituent materials at room temperature (22ºC).

Material	Young's modulus, E^0 (MPa)	Density, ρ (Kg/m^3)	Tensile elongation at break (%)
TPU (Soft material)	230	1230	318
CFR-Nylon (Stiff material)	3800	1170	3

The fabricated parts were then attached by commercial Cyanoacrylates to form a unit cell of the structure.

Testing Method: The bottom surface of the unit cell was fixed to an anodized flat surface, while displacement was applied on the top surface of the structure. ADMET eXpert 8612 mechanical tester with a 20 kN load cell was employed to apply a displacement-driven loading with the rate of one millimeter per second. An intermediary part is 3D printed out of PLA and grabbed by the top grip of the mechanical tester to apply the compressive load directly to the top of the samples. Finally, the temperature increase was applied through an ADMET F-280DT heated chamber. Each sample was tested three times to acquire the data for Figures 5c-e.

Appendix B: Wall Stiffness Formulation

The wall stiffness parameter is calculated based on the compound beam bending. First, the equivalent moment of inertia (I_{eq}) is formulated by replacing the cross-sectional area of the stiffer material with a transformed area that has a wider cross-section and is made of one material, i.e., the softer one (**Figure B1**).

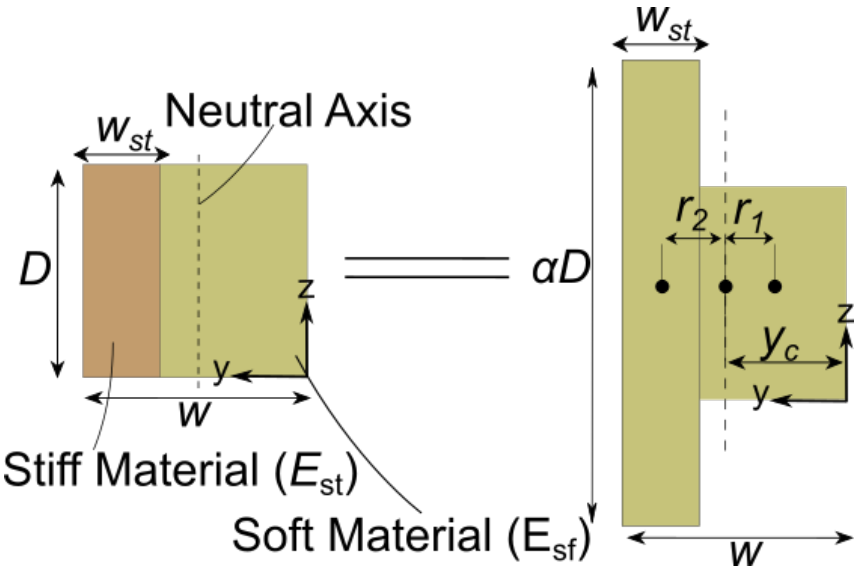

Figure B1. Transformation of the bimaterial cross-section area of the wall to an equivalent single-material geometry.

In Figure B1, α is defined as:

$$\alpha = \frac{E_{st}}{E_{sf}} \tag{S1}$$

where E_{st} represents the elastic modulus of the stiff material and E_{sf} is the elastic modulus of the soft material. The position of the center of the area in the y-direction can be obtained by:

$$y_c = \frac{\frac{D(w-w_{st})^2}{2} + \alpha D w_{st}(w - \frac{w_{st}}{2})}{Dw + Dw_{st}(\alpha - 1)} \tag{S2}$$

Subsequently, the distance between the center of the area of each rectangle to the center of the area of the whole geometry can be written by:

$$r_1 = y_c - \frac{w - w_{st}}{2} \tag{S3}$$

$$r_2 = w - \frac{w_{st}}{2} - y_c \tag{S4}$$

As a result, the equivalent moment of inertia around the *y*-axis is derived as:

$$I_{eq} = \frac{D}{12}(w - w_{st})^3 + \frac{\alpha D w_{st}^3}{12} + D(w - w_{st})^2 r_1^2 + \alpha D w_{st} r_2^2 \tag{S5}$$

Considering the side walls as a cantilever beam with the length of H and a point load at the end, its bending stiffness, *k*, can be written as:

$$k = \frac{3I_{eq}}{H^3} \tag{S6}$$

We divide the flexural stiffness by the length of the strut, L, to make it non-dimensional; hence, the non-dimensional wall stiffness parameter is be obtained by:

$$K_{eq} = \frac{3I_{eq}}{H^3 L}. \tag{S7}$$

Appendix C: Base Material Properties

The storage modulus and the loss factor of the base materials are determined using a Dynamic Mechanical Analyzer (DMA, Q800; TA Instruments) and according to ASTM D5026 standard procedure. Here, the loss factor is defined as $\tan\delta$, where δ is phase lag between stress and strain, and the data is obtained from the DMA analyzer. The test has been performed in a three-point bending mode and the temperature gradually changed from room temperature 22℃ to 100℃. Three samples for each base material (Thermoplastic Polyurethane (TPU) and Carbon-Fiber-Reinforced (CFR) Nylon) were 3D printed and tested. **Figure C1** presents the average results for storage moduli versus temperature, while the standard deviation is shown by highlighted areas. The softening effect can be observed in both materials; however, the trend is quite different. In the case of TPU, we observe a monotonic decrease of storage modulus, while for CFR-Nylon there is a sharp drop between 45℃ and 80℃ that represents glass transition.

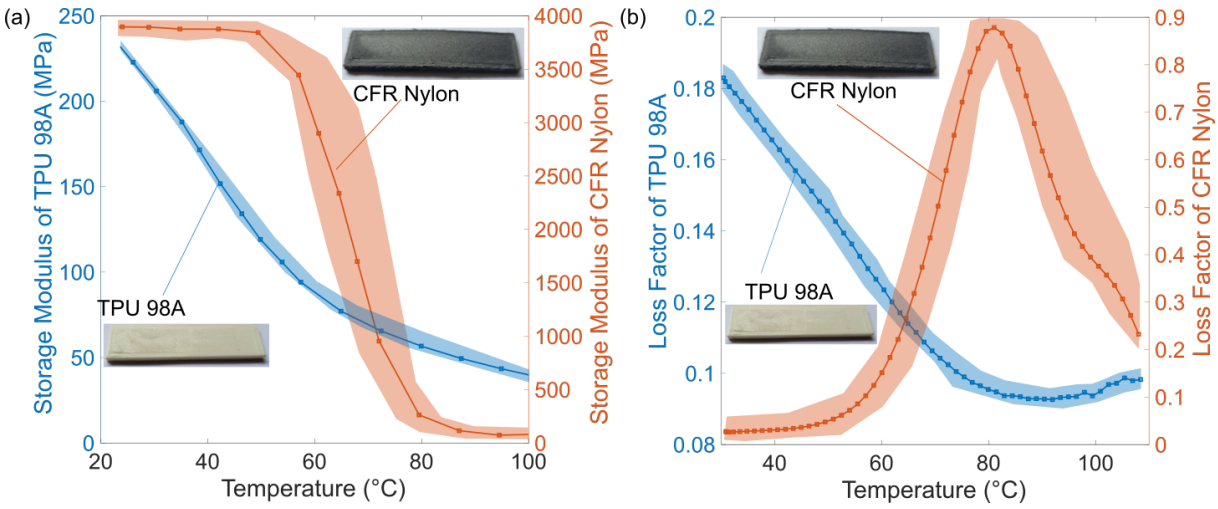

Figure C1. DMA results for TPU 98A and CFR-Nylon. (a) Storage moduli versus Temperature (b) Loss Factor ($tan\,\delta$) versus Temperature

Appedix D:. Effect of Coefficient of Thermal Expansion

The coefficient of thermal expansion is generally not considered in this study because the effect is negligible. In **Figure D1,** we obtained the results of triggering temperature for a unit cell with different coefficients of thermal expansion and following structural dimensions: $n = 2$, $t/L = 0.028$, $H/D = 60$, $\theta = 40°$, $w/L = 0.2$ and $w_{st}/w = 0.6$ using FE simulation. Generally, we can see that by changing the coefficient of thermal expansion of both soft (CTE_{sf}) and stiff (CTE_{st}) materials in a relatively wide range for polymers (0 to $10^{-4}\,°C^{-1}$), the triggering temperature changes slightly; subsequently the effect of thermal expansion may be neglected. A closer look at the results shows that the higher value of CTE for the soft material and the lower value of CTE for the stiff material can generally, increase the triggering temperature of the thermally bistable structure.

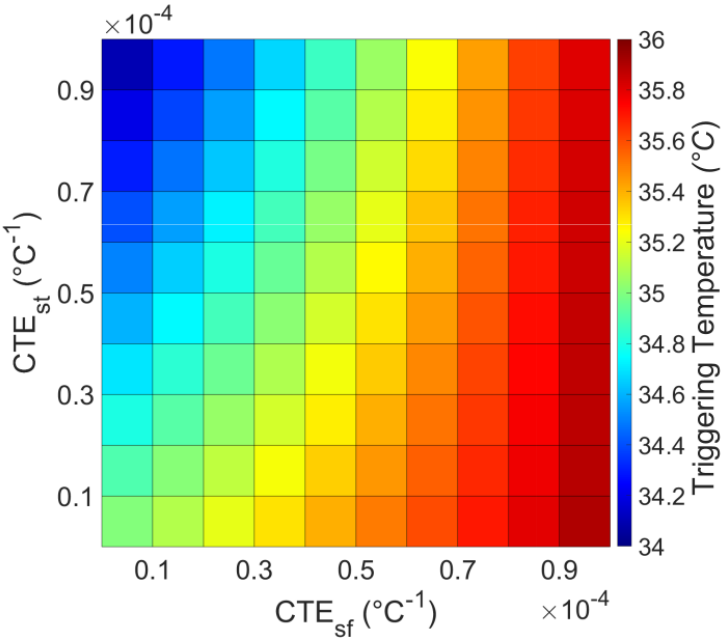

Figure D1. The effect of variation of coefficient of thermal expansion on the triggering temperature based on FE simulation

Appendix E: Manufacturing defects

The snap-through behavior of bistable materials highly depends on the quality of fabrication and consequently, any imperfection caused by the 3D printing or fabrication processes can lead to the deviation between numerical modeling and experimental results. In particular, any possible defects in the form of the inconsistency of strut thickness caused by over or under extrusion of the samples during the FDM 3D printing process may have a significant effect on the force-displacement curve and the snap-through response of the thermally bistable element/structure. **Figure E1** presents the microscopic images of one of the 3D printed samples; we can observe that the thickness of as-built struts has a small variation along the strut length. Effect of over extrusion can be observed at the point of connection of struts to the wall, which leads to variation from the as-designed unit cell model used for numerical modeling through FE.

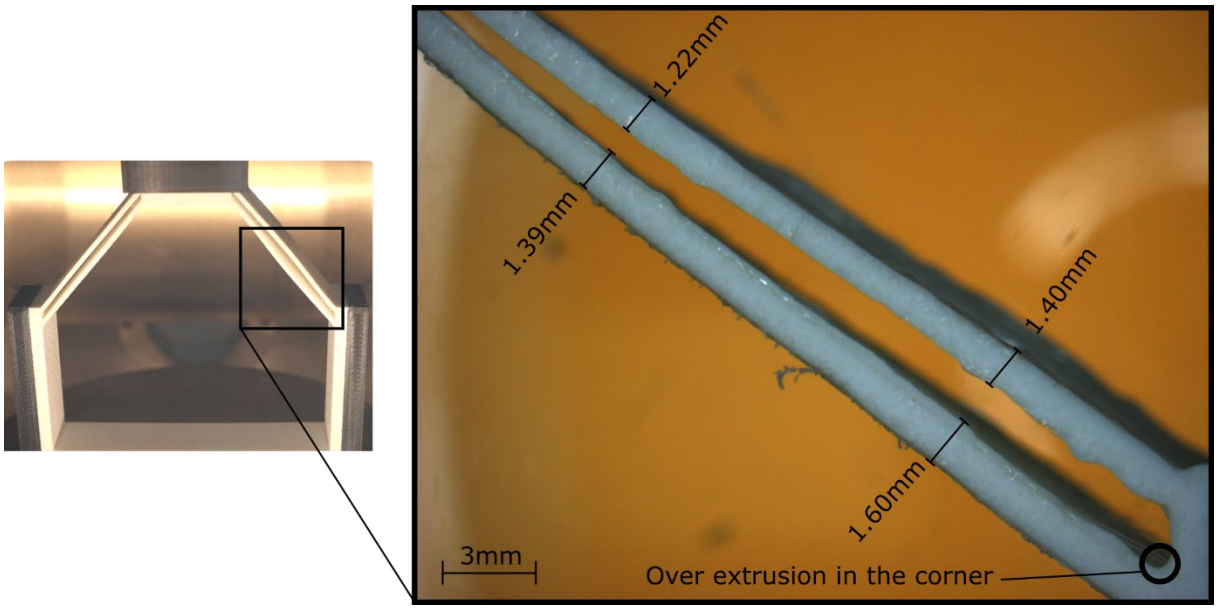

Figure E1. Microscopic image of struts of a 3D printed unit cell with $1.4mm$ strut thickness.

Appendix F: Stress Distribution Throughout the Unit Cell

Increasing the temperature reduces the stiffness of the constituent materials, leading to lower bistability energy. **Figure F1** shows that the stress distribution of the walls depends much more on the applied temperature than the applied deformation. The higher temperature of the wall makes the snapping structure more flexible and reduces the equivalent stiffness parameter (K_{eq}), and consequently transforms the bistable structure to a monostable one.

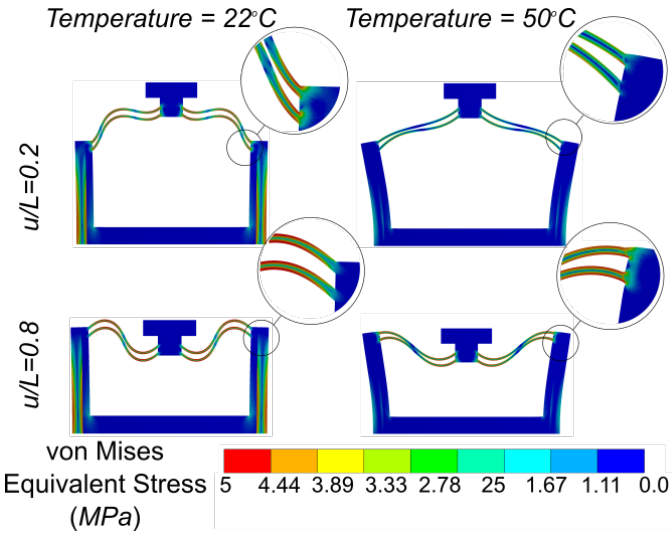

Figure F1. Stress distribution of the unit cell at two different applied deformation and temperature.

Appendix G: Experimental loading and unloading

Figures G1a-b present the experimental force-displacement data for a sequence of loading and unloading presented in Figures 6a-b, respectively. We can see that the reaction force in the case of unloading at room temperature is zero (Figure G1a) as the structure remains in its second stable configuration when the force is removed. Nonetheless, if we increase the temperature before applying the deformation (Figure G1b), the bistability energy will be zero and consequently, the reaction force will be non-zero during the unloading.

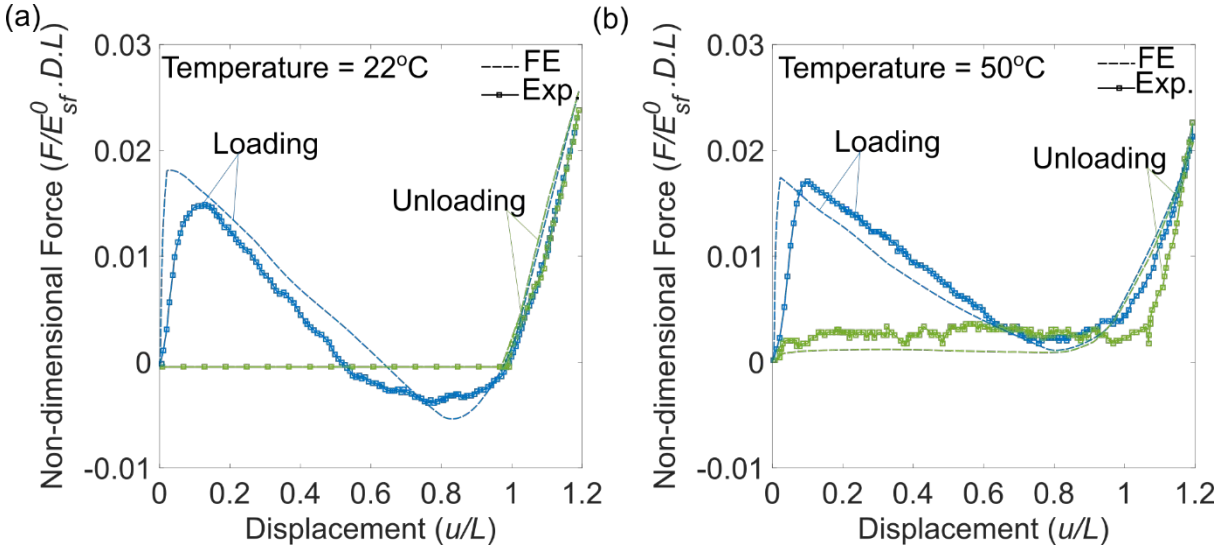

Figure G1. (a) and (b) Force-displacement curves sequence of loading and unloading at room temperature (22 ℃) and an elavated temperature (50 ℃) for the same unit cell.